

An extended Rayleigh model of bubble evolution

Michael E. Glinsky

BHP Petroleum, Houston, Texas 77056

David S. Bailey, Richard A. London, Peter A. Amendt, and Alexander M. Rubenchik

Lawrence Livermore National Laboratory, Livermore, California 94550

Moshe Strauss

Nuclear Research Center, Negev, Beer Sheva, Israel

(Received 24 June 1998; accepted 27 September 2000)

An extended Rayleigh model for laser generated bubbles in water and soft tissue is presented. This model includes surface tension, viscosity, a realistic equation of state, material strength and failure, stress wave emission, and linear growth of interface instabilities. The model is validated by comparison to detailed compressible hydrodynamic simulations using the LATIS computer program. The purpose of this study is to investigate the use of the extended Rayleigh model as a much faster and simpler substitute for the detailed hydrodynamic simulations when only limited information is needed. It is also meant to benchmark the hydrosimulations and highlight the relevant physics. The extended Rayleigh model and the hydrosimulations are compared using both a 1D spherical geometry with a bubble in the center and a 2D cylindrical geometry of a laser fiber immersed in water with a bubble formed at the end of the fiber. Studies are done to test the validity of the material strength and failure, stress wave emission, and the interface instability terms in the extended Rayleigh model. The resulting bubble radii, material damage radii, the emitted stress wave energies, and the size of the interface distortions are compared. Many of the trends found in the hydrosimulations are illuminated by the extended Rayleigh model owing to its relative simplicity. The extended Rayleigh model is very useful since it is accurate over a large range of parameters and it is computationally much faster than the hydrosimulations. © 2001 American Institute of Physics. [DOI: 10.1063/1.1329910]

I. INTRODUCTION

There has been recent interest in using the dynamical effects of small high pressure vapor bubbles for medical applications.¹ The bubbles are created by the expansion of a small volume of water-dominated fluid or soft tissue which has been rapidly heated to high temperature and pressure. It is important to know the most efficient way to cut and break-up tissue with such bubbles. High efficiency is needed to minimize the energy and power of the source and to minimize the amount of residual heat, which can cause unwanted damage. Theoretical modeling of the bubble dynamics is desired in order to reduce the size of parameter space that must be explored experimentally, and to develop a fundamental understanding of the mechanisms.

Vapor bubbles cut and break-up tissue via two primary mechanisms. In the first (expansion) mechanism, which is the focus of this paper, the tissue is broken-up by a shock wave and shear stresses associated with the expansion of the bubble. The second (collapse) mechanism is associated with a shock wave and a fluid jet created upon collapse of a non-spherical bubble. The role of the collapse mechanism in medical applications has been studied recently by other workers.² In the expansion mechanism, the most important quantities desired from a model are the size of the region which experiences material failure (the damaged region), and the efficiency of creating a damaged region of a certain size.

As discussed below, the size of the damaged region is closely related to the maximum bubble size. Bubbles often expand to many times their initial radius. In this case, a 1D spherical model suffices to describe the expansion phase. To describe jet formation on bubble collapse, a 2D axisymmetric model is needed. Since we are mainly interested in the expansion mechanism of tissue damage, we concentrate on 1D spherical models of bubble dynamics. In addition, we present estimates of the growth of perturbations to this symmetry which ultimately lead to the jet formation, and the results of a 2D axisymmetric calculation to support the perturbation calculations.

The vapor bubbles under consideration are similar to cavitation bubbles, whose study has a long rich history, including work by Rayleigh³ and work in the 1940s and 1950s motivated by the need to understand the mechanics of underwater propeller damage caused by cavitation bubbles.⁴ Several books and review articles⁵ summarize the status of bubble research as of the 1970s while some of the more recent work is reported in the papers cited in Ref. 6. Advances associated with sonoluminescence have been discussed most recently.⁷ Research on underwater explosions is also relevant to the present work.⁸ An important result of the previous research is an enhanced Rayleigh model for bubble evolution.

In order to address the medical applications of vapor bubbles, we are motivated to further extend the Rayleigh

model to include material strength and failure and to correctly account for the emitted acoustic energy. The advantages of an extended Rayleigh model (ERM) over a more detailed compressible hydrodynamic model are computational speed and simplicity since the ERM is described by a single ordinary differential equation, while the hydrodynamic model is composed of a set of partial differential equations. Although the ERM is more efficient, it does not give information such as the detailed evolution of the stress wave or shock once it is emitted. It also does not take into account internal structure of the bubble or the more complicated models of material failure. Because of these limitations, it is necessary to compare the ERM to compressible hydrodynamic simulations to verify its accuracy and range of validity.

II. EXTENDED RAYLEIGH MODEL

The extended Rayleigh model describes two regions—the interior of the bubble and the exterior, separated by the bubble wall. The flow is assumed to be spherically symmetric. The exterior material is assumed to be incompressible. Conduction of heat away from the bubble is ignored here since it occurs on a much longer time scale than the bubble dynamics. The processes of conduction and convection are important in determining the ultimate distribution of residual heat in the medium, but this is outside the scope of the current work. The equation that we use to describe the temporal evolution of the bubble is based on the Rayleigh model,³ enhanced by Kirkwood and Bethe,⁸ and Plesset and Gilmore.⁴ We further extend this model to include the addition of heat at the onset of bubble expansion, material strength and failure, a more accurate accounting of the partial reflections of stress waves at the surface of the bubble, and an accurate equation of state. The second order ODE for the position of the bubble wall, R , is

$$\begin{aligned} R\ddot{R}(1 - \dot{R}/c_s) + \frac{3}{2}\dot{R}^2(1 - \dot{R}/3c_s) \\ = h(1 + \dot{R}/c_s) + F \frac{R}{c_s} \dot{h}(1 - \dot{R}/c_s), \end{aligned} \quad (1)$$

where $h \equiv$ enthalpy change between bubble wall and infinity $= \int_{P_0}^P dP/\rho_s$; $F \equiv (\rho_s - \rho_b \dot{R}(c_b - \dot{R}/c_s^2 - \dot{R}^2))/(\rho_b c_b - \dot{R}/c_s + \dot{R} + \rho_s)$; $P_0 \equiv$ pressure at infinity; $c_s \equiv$ sound speed in solid; $c_b \equiv$ sound speed in bubble; $\rho_s \equiv$ solid density; $\rho_b \equiv$ bubble density. The derivation of Eq. (1) including the reflection factor F is presented in the Appendix.

The pressure is given by the equation

$$P = P_b - \frac{2\sigma}{R} - 4\eta \frac{\dot{R}}{R} - Y(\{R(t)\}), \quad (2)$$

where $\sigma \equiv$ surface energy; $\eta \equiv$ viscosity; $Y \equiv$ negative of radial deviatoric stress; $P_b \equiv$ bubble pressure (from equation of state).

Since all stresses discussed in this paper are deviatoric we will usually refer to them simply as stresses for brevity. The definition of Y is the negative of the deviatoric stress. The bubble pressure, P_b , refers to the total gas pressure inside the bubble. We assume that the laser heating generates

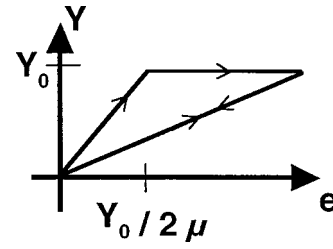


FIG. 1. Stress–strain behavior for material failure model.

all of the bubble gas. Further evaporation of gas into the bubble from the surrounding material is negligible. We use a detailed equation-of-state, as described in Sec. III, to describe the evolution of the internal gas.

The Kirkwood–Bethe⁸ hypothesis has been made in obtaining Eq. (1). This assumes that the kinetic enthalpy in the shock wave emanating from the bubble interior, defined as $h + \dot{R}^2/2$, is much greater than the dissipated enthalpy, defined as $\int TdS$, where S is the entropy. This hypothesis leads to a wave equation for the kinetic enthalpy with velocity $c_s + \dot{R}$. It should be valid for weak shocks, i.e., bubble wall Mach number $= \dot{R}/c_s \ll O(1)$, but since it is a hypothesis it needs to be verified by comparison to detailed dynamic simulations. One can expect it to break down for strong shocks. We have added the reflection factor F to account for partial reflection of the stress wave (or weak shock) at the bubble–solid interface. Note that for small Mach number $F = \rho_s c_s / (\rho_s c_s + \rho_b c_b)$. This shows a complete reflection of the in-going wave (i.e., $F = 1$) for $\rho_b c_b \ll \rho_s c_s$; and a complete transmission of the in-going wave (i.e., $F = 0.5$) for $\rho_b c_b = \rho_s c_s$.

The shear strength and failure has been included by the radial stress term $Y(\{R(t)\})$, which is a function of the complete time history of the bubble wall $\{R(t)\}$. To obtain the expression for this stress it is assumed that the solid is locally linear-elastic with a shear modulus of μ and is incompressible. Failure is assumed to be perfectly plastic. That is, when the failure stress Y_0 is exceeded, the material fails completely and the local stress goes to zero. This gives the expression,⁹

$$Y = 4\mu \left(\frac{R - R_0}{R_0} \right) \frac{(R^2 + R_0 R + R_0^2) R_0}{3R_d^3}, \quad (3)$$

where $R_0 \equiv$ initial unstressed radius; $R_d \equiv \max(R_0, \sqrt[3]{2|R_m^3 - R_0^3|/3\epsilon_d}) =$ radius to which solid has failed; $R_m \equiv$ maximum radius up to time t ; $\epsilon_d \equiv Y_0/2\mu =$ failure strain.

The behavior of the radial stress over a loading cycle is shown in Fig. 1. The solid acts perfectly elastically as the strain of the bubble wall $e = 2(R - R_0)/R$ increases. When the failure stress is reached the material starts to fail out to a radius R_d so that the stress remains clamped at Y_0 . As the strain is decreased, the material as a whole acts again as a

perfectly elastic solid (i.e., it heals) with a reduced shear modulus due to the irreversible material failure.

The linear growth of the interface instability (commonly called the Rayleigh–Taylor instability) can be determined once $R(t)$ is known.¹⁰ The following second order ODE determines the perturbation amplitude ζ_l of the spherical harmonic with mode number l ,

$$\ddot{\zeta}_l + 3\dot{R}\dot{\zeta}_l/R = A_l\zeta_l, \quad (4)$$

where

$$A_l \equiv \frac{[l(l-1) - (l+1)(l+2)\rho_b/\rho_s] \frac{\ddot{R}}{R} - (l^2-1)(l+2) \frac{l\sigma}{\rho_s R^3}}{l + (l+1)\rho_b/\rho_s}. \quad (5)$$

The eigenvalues of this equation are given by

$$\gamma_{l\pm} = -3\dot{R}/2R \pm \sqrt{(3\dot{R}/2R)^2 + A_l}. \quad (6)$$

A qualitative analysis can be made by noting that the perturbation growth scales like $\zeta_l \sim \exp(\gamma_{l\pm}t)$ for constant eigenvalues. The system is unstable to interface instabilities when $\text{Re}(\gamma_{l+}) > 0$. Examining Eq. (6) for $\rho_b \ll \rho_s$, $l \gg 1$, and neglecting the \dot{R} curvature terms, one finds that

$$\gamma_{l+} \sim \sqrt{l\ddot{R}/R - l^3\sigma/\rho_s R^3}. \quad (7)$$

The motion appears to be unstable when $\ddot{R} > 0$, during the recollapse phase, while the density is still at low. However the instability situation is really much more complicated due to several competing terms in Eq. (6), and the rapidly varying conditions during bubble collapse. An accurate analysis requires the integration of Eq. (4) along with the solution of the bubble dynamics equation [Eq. (1)]. This is discussed in Sec. VI.

From Eq. (7) we see that the effect of surface tension is to stabilize the large l -number modes yielding a most unstable mode of

$$l_{\max} \sim R \sqrt{\ddot{R}\rho_s/\sigma}. \quad (8)$$

III. LATIS MODEL

For detailed compressible hydrodynamics simulations we have used the LATIS computer code developed at Lawrence Livermore National Laboratory.¹¹ LATIS is based on LASNEX,¹² a laser-matter interaction code that has over 25 years of usage, including extensive experimental validation, in the field of laser fusion. In addition to the physics that was previously in LATIS, we have added material strength and failure, based on Ref. 13, but with important enhancements described below. LATIS solves the hydrodynamic equations with a Lagrangian finite difference numerical method, as described in the above-cited references. The accuracy ranges between first and second order in space and is second order in time. We have performed zoning studies and determined that the numerical accuracy is 15% for the bubble calculations described below. LATIS is more realistic than the ERM in that it accurately accounts for the emission and propagation of stress wave of arbitrary strength (including shock waves), allows for spatial variation of gas properties within

the bubble, and accounts for spatial dependence of partial material failure. As in the ERM, we do not include heat conduction, since it is negligible during the bubble lifetime.

There are three equations that are used to advance the velocities, strains, and then the stresses in succession. The first is the dynamic equation (a generalization of the fluid momentum equation) given by

$$\rho\dot{\mathbf{v}} = \nabla \cdot (-P\vec{I} + \vec{S}), \quad (9a)$$

where

$$\rho\dot{v}_r = -\frac{\partial}{\partial r}(P - S_{rr}) + \frac{\partial}{\partial z}S_{rz} + \frac{1}{r}(2S_{rr} + S_{zz}),$$

$$\rho\dot{v}_z = -\frac{\partial}{\partial z}(P - S_{zz}) + \frac{\partial}{\partial r}S_{rz} + \frac{1}{r}S_{rz},$$

and P =pressure, \vec{S} =deviatoric stress tensor, \vec{I} =identity tensor, \mathbf{v} =velocity, and ρ =density. Two-dimensional cylindrical coordinates, r and z , are used. The second is the kinematic equation (a generalized equation of continuity) given schematically by

$$\frac{\dot{\theta}}{3}\vec{I} + \vec{e} = \vec{\epsilon}(\mathbf{v}, \nabla\mathbf{v}), \quad (9b)$$

where \vec{e} =deviatoric strain tensor, θ =fractional volume change, and ϵ is a tensor function of velocity and its gradient. Equation (9b) can be expressed explicitly by writing out the tensor components of the left-hand side,

$$\dot{\theta} = \frac{\partial v_r}{\partial r} + \frac{\partial v_z}{\partial z} + \frac{v_r}{r},$$

$$\dot{e}_{rr} = \frac{1}{3} \left(2 \frac{\partial v_r}{\partial r} - \frac{\partial v_z}{\partial z} - \frac{v_r}{r} \right),$$

$$\dot{e}_{zz} = \frac{1}{3} \left(2 \frac{\partial v_z}{\partial z} - \frac{\partial v_r}{\partial r} - \frac{v_r}{r} \right),$$

$$\dot{e}_{rz} = \frac{1}{2} \left(\frac{\partial v_r}{\partial z} + \frac{\partial v_z}{\partial r} \right).$$

The third equation is a generalization of Hooke's law given by

$$-\dot{P}\vec{I} + \dot{\vec{S}} = K(\dot{\theta} - \dot{\theta}_{\text{in}})\vec{I} + 2\mu(\dot{\vec{e}} - \dot{\vec{e}}_{\text{in}}) + \dot{\vec{S}}_{\text{rot}}, \quad (9c)$$

where K =bulk modulus, μ =shear modulus, $\dot{\theta}_{\text{in}}$ =inelastic volume change, $\dot{\vec{e}}_{\text{in}}$ =inelastic strain tensor, and $\dot{\vec{S}}_{\text{rot}}$ is a small correction accounting for coordinate rotations which may occur due to the Lagrangian hydrodynamic method,

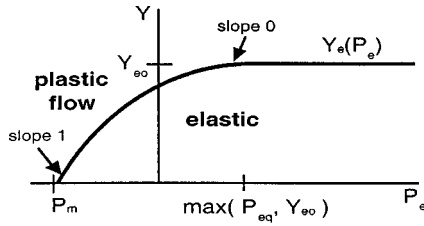
$$[\dot{\vec{S}}_{\text{rot}}]_{rr} = 2S_{rz}\omega_{rz},$$

$$[\dot{\vec{S}}_{\text{rot}}]_{zz} = -2S_{rz}\omega_{rz},$$

$$[\dot{\vec{S}}_{\text{rot}}]_{rz} = 2(S_{zz} - S_{rr})\omega_{rz},$$

where

$$\omega_{rz} = \frac{1}{2} \left(\frac{\partial v_r}{\partial z} - \frac{\partial v_z}{\partial r} \right) = r_z \text{ rotation frequency}. \quad (10)$$


 FIG. 2. Yield surface, $Y_e(P_e)$.

If the pressure is less than a certain minimum value (P_m , which is negative) then the pressure will relax to the minimum value because of an increase in inelastic strain. That is, when the failure stress is reached, defects will grow to clamp the pressure at that negative value. When the pressure goes positive, the inelastic strain will be healed pushing the pressure back to zero. Once all of the inelastic strain has been healed (that is all void space collapsed) the material will be able to support positive pressure. This is ensured by not allowing the inelastic strain to be less than zero. In order to model this effect, the values of the inelastic changes to the strains and volume are chosen such that the pressure relaxes to the minimum pressure P_m if it is less than P_m and to zero if it is greater than zero, and that the deviatoric stress invariant

$$Y = \sqrt{2\vec{S}:\vec{S}/3} \quad (11)$$

relaxes to its limit $Y_e(P_e)$ for values greater than $Y_e(P_e)$, where the effective pressure is

$$P_e = P - \sqrt[3]{|\vec{S}|/16},$$

$$\vec{S}:\vec{S} = 2(S_{rr}^2 + S_{zz}^2 + S_{rz}^2 + S_{zz}S_{rr}),$$

and

$$|\vec{S}| = (S_{rr} + S_{zz})(S_{rz}^2 - S_{rr}S_{zz}).$$

We have defined Y with a factor of $\sqrt{2/3}$ rather than the usual $\sqrt{3/2}$ to be consistent with the definition of Y in Eq. (3). With a yield strength of Y_0 we get an effective pressure of Y_0 added to the bubble by the material strength. The yield surface $Y_e(P_e)$ that we use is shown schematically in Fig. 2.

The inelastic change θ_{in} is limited so that the inelastic volume, V_{in} , will be between zero and the total volume, V . All the deviatoric stresses are scaled by the same factor so that Y will have the desired value.

The damage index, ϵ_D , is calculated as

$$\epsilon_D = \min\left(1, \frac{e_p}{e_0} + \frac{\theta_{in}}{\theta_0}\right), \quad (12)$$

where e_0 is the shear strain threshold and θ_0 is the tensile strain threshold. These thresholds are the critical points where the disconnected flaws (such as voids or cracks) coalesce into a large one and the material ‘‘breaks.’’ The plastic strain is defined as

$$e_p \equiv \int |de_{in}|, \quad (13)$$

where

$$e_{in} = \sqrt{2\vec{e}_{in}:\vec{e}_{in}/3}. \quad (14)$$

The index for tensile failure is θ_{in} —the maximum percentage void volume, $\max(V_{in}/V)$ if the tensile damage is not allowed to heal, and V_{in}/V if the tensile damage is allowed to heal. The density used to calculate the pressure is taken to be the mass in the zone divided by the volume of the cell that is not void, $V - V_{in}$.

The effect of the damage is to decrease both the absolute value of the minimum pressure P_m and the shear yield limit Y_{eo} to $P_{mo}(1 - \epsilon_D)$ and $Y_{eoo}(1 - \epsilon_D)$, respectively. Here P_{mo} and Y_{eoo} are constants that characterize the nucleation of the microscopic defects which cause the material failure. This leaves one with the following expressions for the time derivatives for the inelastic strains:

$$-K\dot{\theta}_{in} = \begin{cases} \frac{1}{\tau}[P] & \text{if } P > 0 \\ 0 & \text{if } 0 > P > P_m \\ \frac{1}{\tau}[P - P_m] & \text{if } P < P_m \end{cases}, \quad (15)$$

$$2\mu\dot{e}_{in} = \begin{cases} \frac{\vec{S}}{\tau Y}[Y - Y_e] & \text{if } Y > Y_e \\ 0 & \text{if } Y < Y_e \end{cases}, \quad (16)$$

where the relaxation time is governed by the equation

$$\frac{d\tau}{dt} = \begin{cases} -\frac{1}{\tau_o}[\tau] & \text{if } \epsilon_D = 1 \\ -\frac{1}{\tau_o}[\tau - \tau_o] & \text{if } \epsilon_D < 1 \end{cases}, \quad (17)$$

and the basic relaxation time is

$$\tau_o = \max\left(\frac{\text{zone area}}{Ac_s \min(\Delta r, \Delta z)}, \tau_{oo}\right). \quad (18)$$

This formulation is designed both to approximately model the growth of flaws in the material and to limit numerical noise in the solution of the hydrodynamic equations. This is in lieu of a rate dependent model for the stress moduli. The first term is the sound transit time across the zone and prevents an instability in the numerical integration of the equations of motion. The second term is a zonal user supplied time that accounts in an empirical way for the rate dependence of the material failure. The relaxation of τ from τ_o to 0 when $\epsilon_D = 1$ helps model the coalescence of voids. The time constant should be chosen to be the characteristic time for the disconnected flaws to grow from the size on which they are nucleated to the size of the interflaw spacing.

The bulk modulus is derived from the equation of state (EOS). The shear modulus is supplied by the user. Two different EOSs for water were used in this work. The first is a table calculated using QEOS.¹⁴ This table is valid over a large range in both temperature and density but is not very accurate around the vapor dome. The second EOS was based on the NBS steam tables.¹⁵ Although this table is very accurate around the vapor dome it has a limited range of validity.

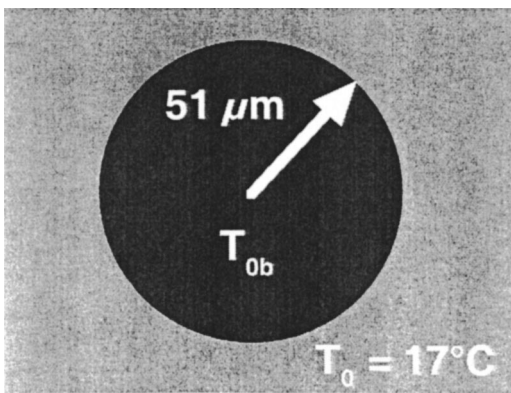


FIG. 3. Simulation geometry.

IV. RESULTS OF BUBBLE EVOLUTION AND STRESS WAVE EMISSION SIMULATIONS

Comparisons of the stress wave emission between the extended Rayleigh model and the detailed dynamic simulations with LATIS have been made. The geometry is shown in Fig. 3. A large (practically infinite) volume of water is initially at temperature $T_0 = 17^\circ\text{C}$, pressure $P_0 = 10$ bar, and liquid density (≈ 1 g/cm³). A spherical region is then instantaneously heated at constant density to temperatures (T_{0b}) ranging from 200 to 500 °C. For both models, the QEOS equation-of-state is used for the water and we assume that there is no surface tension or viscosity. The radius as a function of time is monitored as well as the energy that is emitted during the initial expansion and during the first collapse. The temporal histories of the bubble radii, shown in Fig. 4, compare quite well. Both models show no bounce of the bubble for an initial temperature of 200 °C, only one bounce for 300 °C, and many bounces for 400 °C and 500 °C. The temperature (and pressure) inside the bubble varies with time in the opposite sense to the radius: as the bubble increases the temperature drops, and vice versa. This results from the fact that the bubble evolution is nearly adiabatic.

As shown in Fig. 5(a), the maximum bubble radius for the first expansion for the extended Rayleigh model is 20% less than for the LATIS simulations but there is the same trend of increasing maximum radius with increasing bubble temperature. The discrepancy in the bubble radius disappears for

the second expansion. Both the magnitude and the functional form of the maximum bubble radius match quite well. The efficiency of acoustic radiation during the initial expansion and during the first collapse [Fig. 5(b)] show the same trends as the maximum bubble radius—there is more energy radiated by the extended Rayleigh model during the first expansion but less during the first collapse.

The different bounce behavior of the high and low initial temperature bubbles evident in Fig. 4 can be understood from the pressure–volume trajectories followed by material inside the bubble. In all cases, the evolution is approximately adiabatic. As illustrated in Fig. 6, the adiabats have a steep pressure decline from the initial state and a flat part where the water exists in a two-phase (liquid-gas) state. During the expansion and collapse cycle, bubble energy is lost by acoustic emission to the exterior region [see Fig. 5(b)]. This loss results in a lower pressure–higher volume position reached upon recollapse, as indicated by the diamonds in Fig. 6. Hence, the second expansion is less energetic than the first in both cases. The critical difference between the two cases is the level of the two-phase pressure compared to the background pressure. In the 400 °C case, the two-phase pressure is about 18 bar, larger than the background pressure of 10 atm, while for the 200 °C case the two phase pressure is 3 bar, lower than the background pressure. Since expansion is driven only when the bubble pressure is larger than the background pressure, the lower temperature bubbles do not experience any drive from the two-phase portion of the trajectory and therefore show a much weaker bounce than the higher temperature bubbles.

The role of shock waves and their treatment in the two models is discussed here. Significant shock waves are created by the initial bubble expansion and on subsequent bubble collapses. The inward propagating shocks tend to stay trapped within the bubble. The emission of shock waves upon bubble expansion and collapse is included in both the ERM and LATIS model, whereas detailed tracking of the shocks is done only in the LATIS model. Previous calculations of the emission and tracking of shocks has been discussed in the context of sonoluminescence by Roberts and Wu.⁷

The effect of shock wave emission is found to be generally very important. For example in the 200 °C case illus-

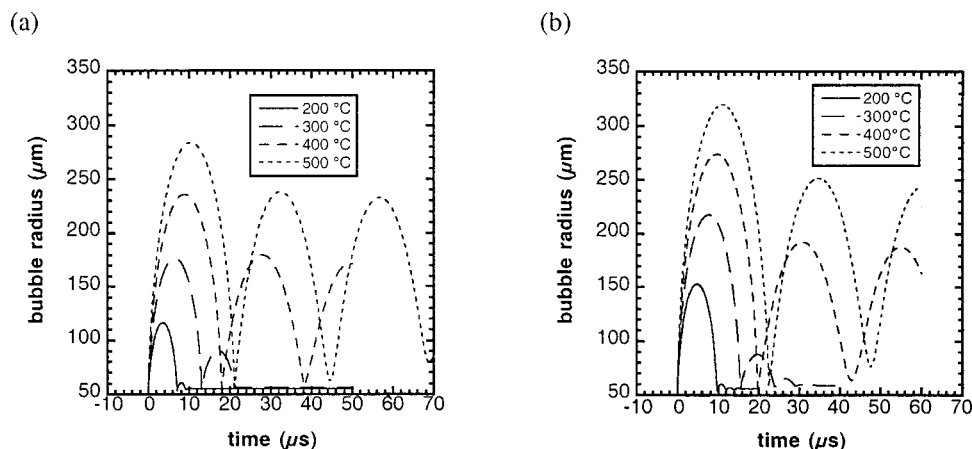


FIG. 4. Bubble radius as a function of time for (a) the ERM and (b) for LATIS.

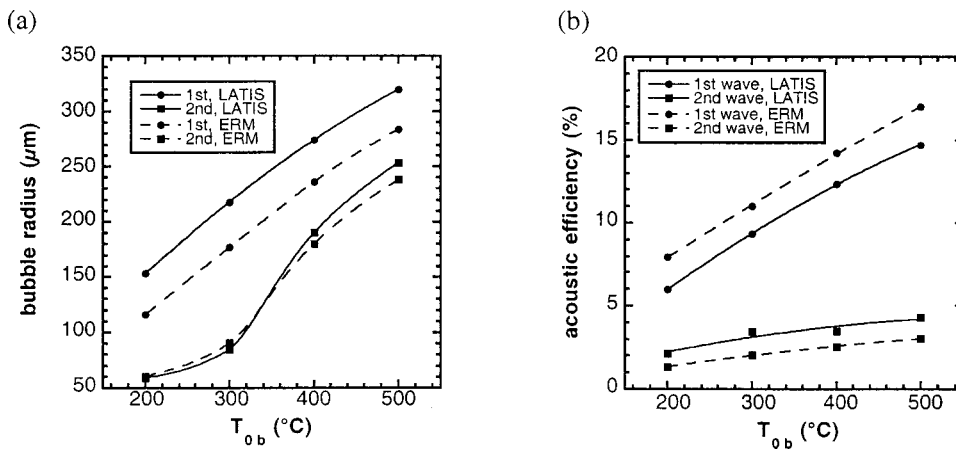


FIG. 5. (a) Maximum bubble radius as a function of initial bubble temperature for the first and second expansion for the extended Rayleigh model (ERM) and LATIS; and (b) the acoustic efficiency as a function of the peak bubble temperature for the first and second emission of acoustic waves. The efficiency is defined as the energy emitted into the acoustic wave divided by the thermal energy required to heat the bubble up to its initial temperature.

trated in Fig. 4, almost all of the energy in the first bubble oscillation is dissipated as shock energy during the first collapse. The good agreement between the two models indicates that the approximate treatment of the shock emission in the ERM is adequate to predict the bubble dynamics with shock emission. To achieve this accuracy we have found that both the terms in \dot{R}/c_s in Eq. (1) resulting from the Kirkwood–Bethe hypothesis as well as the correction to the reflection factor (F) described in the Appendix must be included in the ERM. If one drops the \dot{R}/c_s in the last term of Eq. (1) there is a 25% or greater discrepancy between the ERM and LATIS in the energy radiated into the shock. For the cases which we consider, the maximum value of \dot{R}/c_s is 0.5. These large values of \dot{R}/c_s is one of the reasons that we felt it was necessary to benchmark the ERM against a compressible hydrodynamic model. Dropping the correction to the reflection factor was found to lead to a factor of 2 discrepancy in the amount of shock energy radiated and in the maximum radius.

Tracking the shock waves inside the bubble was found not to be important to determine the bubble radius. This is indicated by the good agreement between the results of the two models in Fig. 4. In the ERM, the internal shock waves are assumed to be trapped and dissipated. In order for them to escape they would have to be at the boundary of the bubble when it collapses, a very unlikely occurrence. There is also a much smaller transmission coefficient out of the interior upon recollapse due to the energy that was initially radiated into a shock (the bubble interior will not reach solid density on collapse). The verification of this picture is another reason for the comparison of the ERM to the detailed compressible hydrodynamic model.

V. RESULTS OF MATERIAL FAILURE SIMULATIONS

The material strength and failure term in the ERM is tested using the same 1D spherical geometry shown in Fig. 3. The initial bubble temperature is 400 °C for all the simulations in this section. The EOS is based on the NBS steam tables. The first case is with no material strength or failure. The ambient pressure P_0 is 10 bar. The bubble radii calculated from the ERM and LATIS are shown in Figs. 7(a) and 7(b), respectively. The agreement between the two models is incredibly good. For the second case, shown in Figs. 8(a) and 8(b), the ambient pressure is reduced to $P_0 = 1$ bar, the shear modulus μ is set to 300 bar, the shear failure stress Y_0 to 10 bar and the shear failure strain e_0 to 8×10^{-5} . These parameters model a perfectly elastic material which fails immediately and completely (since e_0 is so small) when the failure stress is exceeded. The calculations of the bubble radius and the maximum radius to which the material has completely failed agree well, with the LATIS calculations indicating about 4% larger damage radius than the ERM. We note that the maximum bubble radii are approximately equal for the two cases shown in Figs. 7 and 8. The material strength and failure has acted as an effective ambient pressure of 10 bar. For the third and final case, the complete failure is delayed by using a failure strain e_0 of 0.24. Results from a LATIS simulation are shown in Fig. 9. It is not possible to do the equivalent simulation using the ERM because the material failure model in the ERM includes only a failure radius separating the failed region on the inside from the elastic region

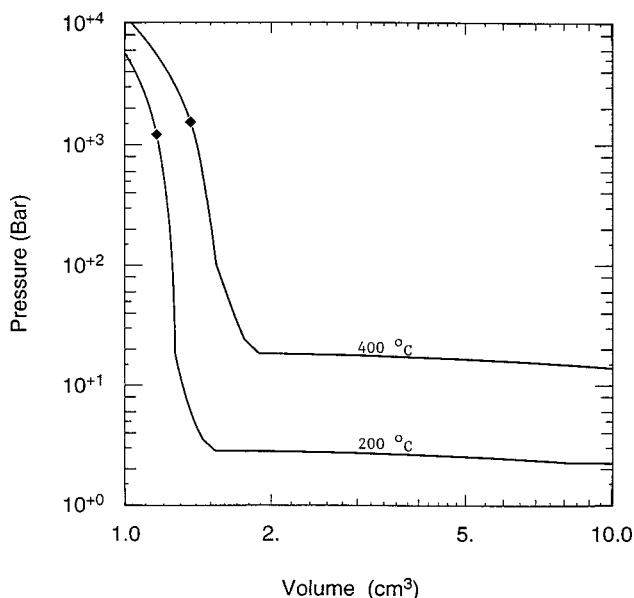


FIG. 6. Adiabats in the P - V plane for initial temperatures of 200 and 400 °C. The initial points are at $V=1$ and high pressure. The highest points reached on bubble collapse are indicated by diamonds.

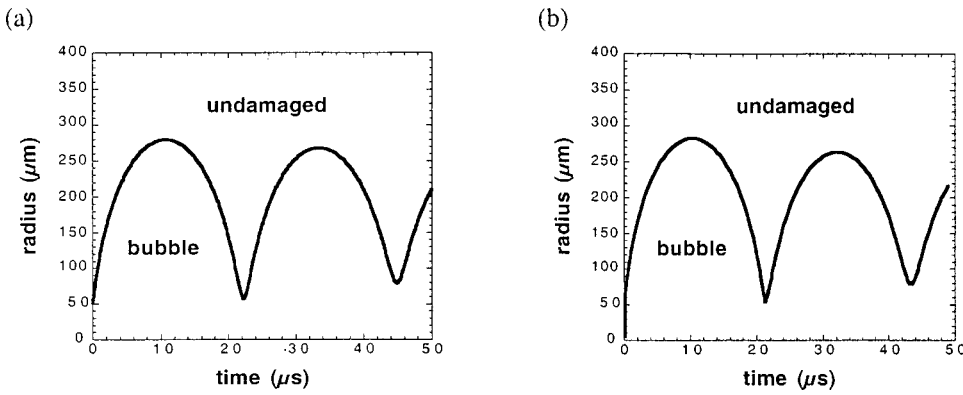


FIG. 7. Bubble radius as a function of time for (a) the extended Rayleigh model and (b) for LATIS. Case 1: $P_0 = 10$ bar, $Y_0 = 0$, $\mu = 0$.

outside. It does not allow partial failure as is found in the general case, e.g., for $e_0 = 0.24$. Figure 9 displays three curves giving the results of this simulation. The first is the bubble radius. The maximum radius is reduced 30% compared to case 2 shown in Fig. 8(b) by delayed coalescence, which has raised the effective applied pressure above 10 bar. The second curve is the radius to which the material has completely failed. The third curve delineates the dividing line between the region of partial failure and no failure. Figure 10 shows examples of typical stress-strain curves for the three regions shown in Fig. 9. The first is that of a perfectly elastic stress-strain curve (undamaged material). The second is that of material that has started to undergo failure but has not yet totally failed. The final curve is that of material that has totally failed and will no longer support any stress.

The next three figures (Figs. 11–13), show the details of the evolution of the three LATIS simulations just discussed. Three quantities are displayed. The first is the density multiplied by a factor of 3, chosen for convenience of display. The other two quantities are the \log_{10} of the pressure P and the negative of the radial stress, $-S_{rr}$, measured in bar. Negative quantities correspond to negative values of the quantities. The first case, Fig. 11, shows the pressure wave moving away from the bubble. It leaves behind the pressure profile predicted by the Rayleigh model. The second case demonstrates the effect of material strength and failure. Figure 12 shows the spatial distribution of the pressure, density, and (deviatoric) radial stress at several times. As the acoustic wave moves away from the bubble, it has a much greater

pressure than radial stress. This is because of the small shear modulus, 300 bar, compared to the bulk modulus of water, 22 kbar. The radial shear stress is still enough in this wave to cause failure of the material out to 200 μm as indicated by the zero value of the radial stress out to this radius at 0.2 μs . For longer times the stress builds up to the failure stress of 10 bar as one approaches the bubble. At this point the material can no longer support radial stress; the material fails and the stress is transferred to a pressure of 10 bar which is communicated to the bubble wall. Since the total stress is continuous, the deviatoric part outside the region of failure will be taken up by the pressure inside the region of failure, as illustrated in the region near 950 μm in Fig. 12(c). Also note that the deviatoric radial stress is approximately equal in magnitude to the pressure for the latter time bubble evolution seen in Fig. 12(c). The radius of damaged material is extended to almost 1 mm by the bubble motion.

The final case, Fig. 13, demonstrates the effect of gradual failure. The stress pulse propagates out of the problem causing some degree of damage to a 250 μm radius. This is indicated by the radial stress being clamped at 10 bar in Fig. 13(b). During the longer time bubble evolution, Fig. 13(c), one can see the radial stress build up to a maximum value of 10 bar as the bubble wall is approached from large radii. As one further approaches the bubble wall this stress decreases to zero as the material totally fails and the stress is transferred to a pressure of 20 bar that is communicated to the bubble wall. It is this increased pressure which is responsible for the decreased bubble radius.

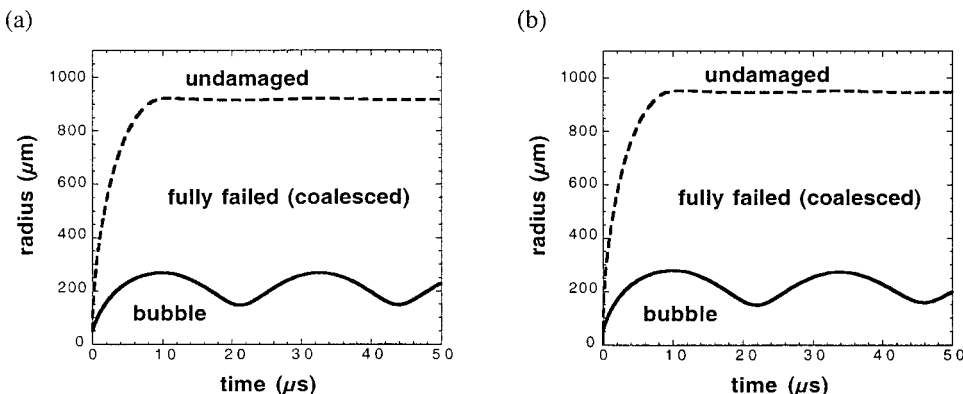


FIG. 8. Bubble radius as a function of time for (a) the extended Rayleigh model and (b) for LATIS. Case 2: $P_0 = 1$ bar, $Y_0 = 10$ bar, $\mu = 300$ bar, and $e_0 = 8 \times 10^{-5}$. Solid line is the bubble radius. Dotted line is the maximum radius to which the material has failed.

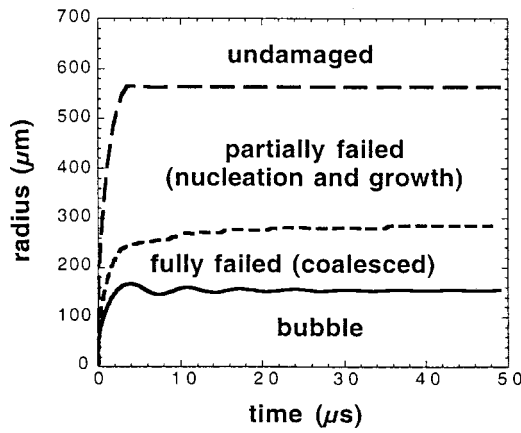


FIG. 9. Bubble radius as a function of time for LAVIS. Case 3: $P_0=1$ bar, $Y_0=10$ bar, $\mu=300$ bar, and $e_0=0.24$. Solid line is the bubble radius. Dotted line in the maximum radius out to which the material has totally failed. Dashed line is the radius out to which there is some failure.

VI. RESULTS OF INTERFACE INSTABILITY SIMULATIONS

The growth of interface instabilities has been studied using the same geometry shown in Fig. 3. The ambient pressure P_0 was 1 bar, the initial bubble temperature was 500 °C, the surface tension σ was 70 erg/cm², and the equation of state was QEOS. The assumed surface tension is appropriate to our idealized scenario in which the temperature profile has a discontinuity at the bubble surface. In a real situation with a smooth temperature profile, the surface tension may be much less since the liquid just outside the bubble would be heated to a temperature near boiling. In either case, the surface tension is not a very important effect. We assume that $\delta_l \ll R$, in accordance with Plesset.¹⁰ We also maintain the assumption of no heat conduction and assume that the vapor pressure inside the bubble is small, as discussed in Sec. II. For the particular case under consideration, the assumption of no heat conduction is expected to be valid for mode-numbers less than about $l=130$. This results from the fact that the conduction heat transport time scale across a distance equal to the wavelength of the mode is longer than the bubble collapse time (10 μ s) for these modes. For smaller bubbles, conduction might be important at smaller mode numbers.

The growth of the instabilities is shown in Fig. 14. In Fig. 14(a) we show the growth of the $l=10$ and $l=100$ modes, using the WKB approximation, namely, $\zeta_l = \zeta_{l0} \exp[\int \gamma_{l+} dt]$, with eigenvalues found from Eq. (6). This approximation is valid when the time rate of change of the

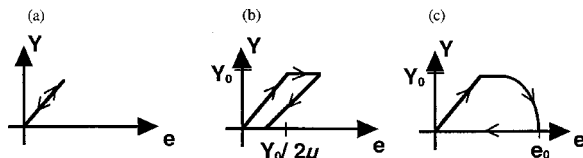


FIG. 10. Examples of stress-strain relationship for (a) perfectly elastic and undamaged material, (b) material which has partially failed, and (c) material which has totally failed.

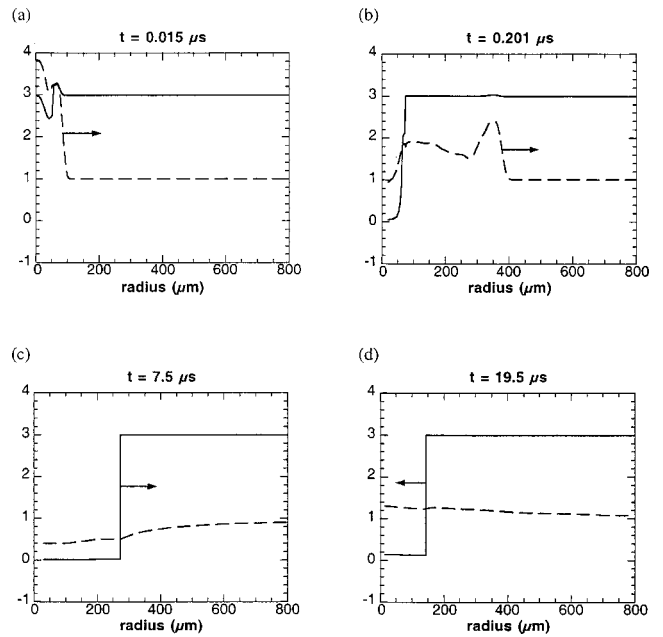


FIG. 11. Density (ρ , solid line), pressure (P , dashed line) vs radius. Density is multiplied by three with units of g/cm³. The pressure is displayed as $\log_{10}(P)$, where P is in bar. Each panel is a snapshot at the time indicated. The arrows indicate direction of motion. The material parameters are $P_0=10$ bar, $\mu=0$, $Y_0=0$.

coefficients is less than the instability growth rate, $1/|\gamma_+|$, and is much easier to calculate than the solution of Eq. (4), which is more generally valid. The $l=10$ mode grows more than a decade during each collapse of the bubble. The $l=100$ mode is stabilized by the surface tension which resists

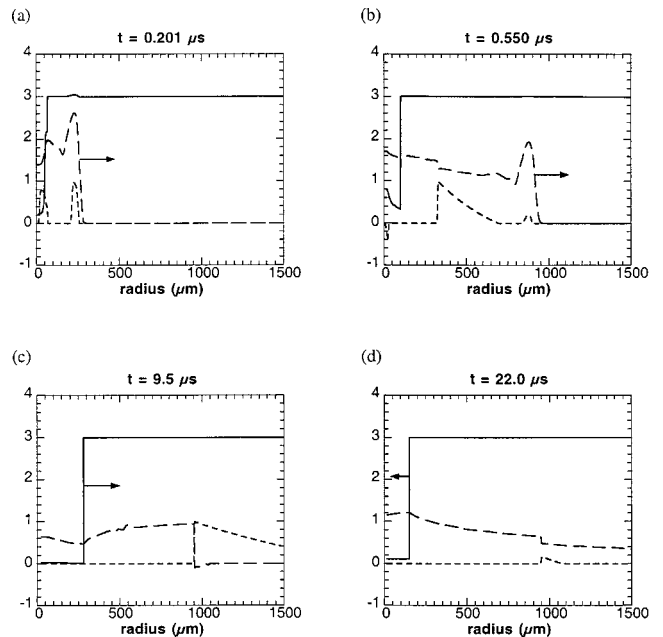


FIG. 12. Density (ρ , solid line), pressure (P , dashed line), and radial stress ($-S_{rr}$, dotted line) vs radius. Density is multiplied by three with units of g/cm³. The pressure is displayed as $\log_{10}(P)$, where P is in bar. The radial stress is displayed as $\log_{10}(-S_{rr})$, where S_{rr} is in bar. Each panel is a snapshot at the time indicated. The arrows indicate direction of motion. The material parameters are $P_0=1$ bar, $\mu=300$ bar, $Y_0=10$ bar, $e_0=8 \times 10^{-5}$.

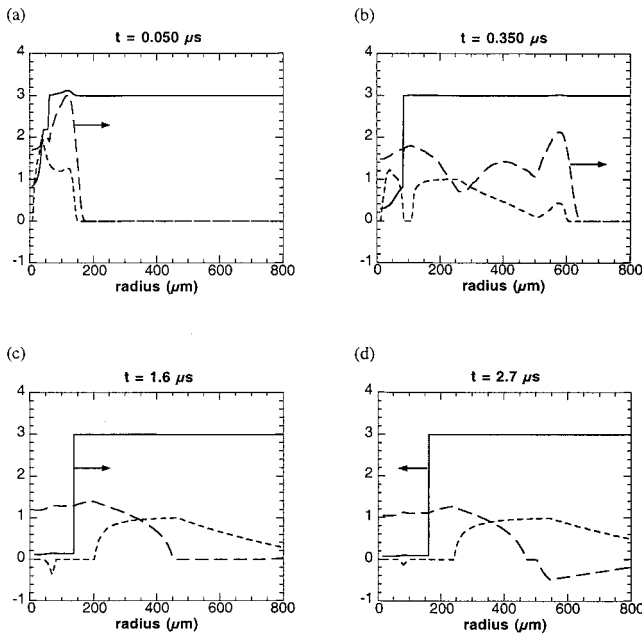


FIG. 13. Density (ρ , solid line), pressure (P , dashed line), and radial stress ($-S_{rr}$, dotted line) vs radius. Density is multiplied by three with units of g/cm^3 . The pressure is displayed as $\log_{10}(P)$, where P is in bar. The radial stress is displayed as $\log_{10}(-S_{rr})$, where S_{rr} is in bar. Each panel is a snapshot at the time indicated. The arrows indicate direction of motion. The material parameters are $P_0=1$ bar, $\mu=300$ bar, $Y_0=10$ bar, $e_0=0.24$.

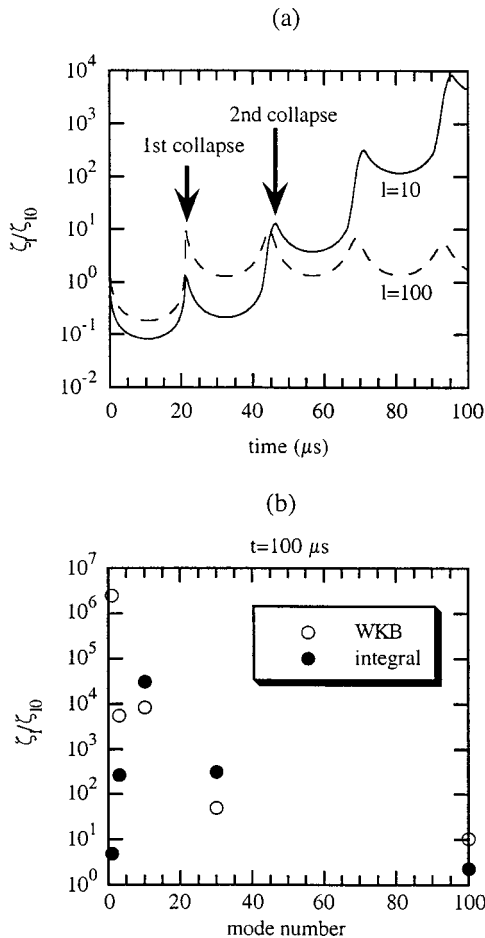


FIG. 14. Growth of the interface instability is shown by the size of the mode normalized by its initial amplitude ξ_l/ξ_{10} . (a) Mode amplitude vs time as predicted by the WKB approximation. (b) Maximum-in-time amplitude vs mode number. The filled circles are determined by solving Eq. (4). The open circles are the result of the WKB approximation.

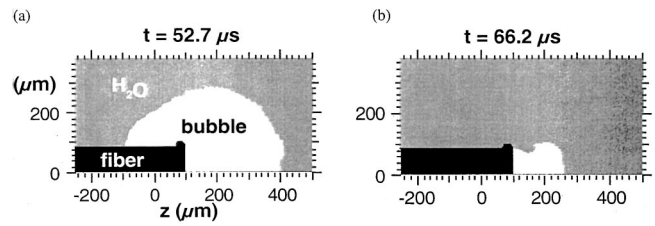


FIG. 15. 2D LATIS simulation of bubble evolution displaying an $l=1$, bubble and spike instability.

surface perturbation. The behavior of the instability as a function of mode number is demonstrated in Fig. 14(b). There we show the maximum growth over time vs mode number, using two levels of approximation. The first is the WKB approximation as used for Fig. 14(a). The second level of approximation uses the solution of Eq. (4), a second order ODE with time varying coefficients. This is more accurate than the WKB approximation. For small l , the maximum instability occurs for small R , $\ddot{R} < 0$, and $\rho_b < \rho_s$, but more importantly, when the time rate of change of the coefficients is large. This is the reason for the discrepancy between the two approximations seen in Fig. 14(b) at small l . On a close examination of the evolution of Eq. (4) for $l=1$, it is found that the mode can grow to the amplitude predicted by the WKB approximation during the first collapse, but the complicated evolution prevents it from growing further. It is apparent that the growth of low mode number instabilities is complicated. The more precise treatment, using Eq. (4) is necessary to correctly predict the growth rates for these modes. For higher modes, the WKB approximation does an adequate job. Note that the maximum instability in the solution of Eq. (4) is for $l=10$ as predicted by Eq. (8). This WKB-based prediction holds for these higher modes.

All modes up to $l=10$ were found to be significantly unstable. There are two important seeds for these instabilities. The first is the nonspherical symmetry imposed by a laser fiber which will seed the $l=1$ mode with at least a few percent amplitude. The second is the presence of a material interface such as a vessel wall. The reflection of the acoustic radiation off of this interface and the subsequent imprint on the vessel wall would be expected to seed a significant $l=2$ perturbation. The growth factors shown in Fig. 14 are quite large and might be expected to alter the bubble evolution. Without instability, the bubble bounces more than 10 times. Since these modes will grow about a decade per collapse it is unlikely that the bubble will be able to bounce more than once or twice.

To further address the role of instabilities in the dynamics of laser generated bubbles we have performed a two-dimensional LATIS simulation.¹⁶ This simulation accounts for the nonspherical creation of a bubble. In the LATIS simulation, 0.312 J of energy is deposited in a 12 μm layer at the end of a laser fiber. The shape of the bubble is shown in Fig. 15 at two times. The rigid-nature of the fiber acts to continuously drive perturbations from a spherical flow in the surrounding water. The fiber predominantly drives the $l=1$ mode with a perturbation of at least a few percent. This leads

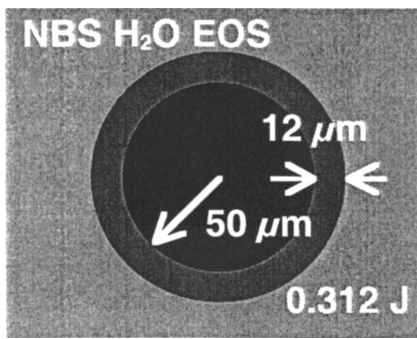


FIG. 16. Geometry used for the ERM to compare to the 2D LATIS simulations.

to the classic bubble and spike shape¹⁷ with Kelvin–Helmholtz roll-up, seen at $66 \mu\text{s}$ in Fig. 15(b).

An extended-Rayleigh model simulation has been done for comparison to the 2D LATIS simulation. The geometry for the ERM is shown in Fig. 16. Outside of a $50 \mu\text{m}$ hard core, 0.312 J is deposited into a $12 \mu\text{m}$ shell. This geometry reproduces both the initial surface area and volume of the 2D calculation. The hard core is a zero displacement boundary. It is used to mimic the effect of a rigid optical fiber. The growth of the $l=1$ mode is shown in Fig. 17. There are significant differences between the 2D LATIS calculation and the ERM calculation. The LATIS calculation has a strong persistent 2D perturbation (the fiber), which continuously drives the bubble dynamics, whereas the ERM model has only an initial perturbation of small amplitude. Despite these differences, a qualitative agreement in the behavior is seen between the two models. The size of the $l=1$ mode is predicted by the ERM to grow by more than a decade during the bubble collapse (Fig. 17) in qualitative agreement with the growth of the bubble and spike seen in the 2D LATIS simulation [Fig. 15(b)]. Thus the results of the 2D simulations combined with those of the ERM support the notion that the Rayleigh–Taylor instability can be important in the bubble

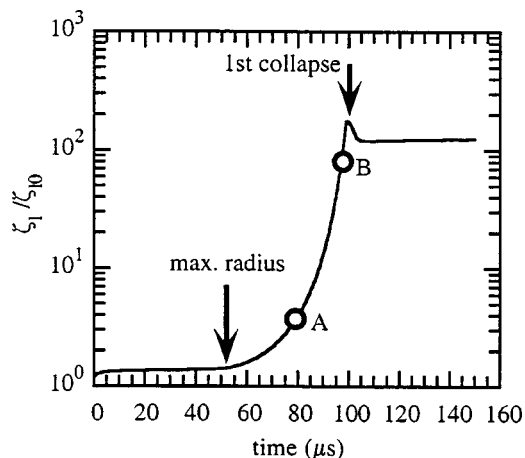


FIG. 17. Growth of the interface instability as a function of time as predicted by the ERM and the WKB approximation. This is for the geometry shown in Fig. 16. Point A corresponds to the 2D LATIS simulation in Fig. 15(a). Point B corresponds to the 2D LATIS simulation in Fig. 15(b).

dynamics during the collapse phase and can limit the number of bubble bounces.

VII. DISCUSSION AND CONCLUSIONS

We have presented an extended Rayleigh model for the dynamics of laser generated vapor bubbles. The extensions beyond previous work include the addition of heat at the onset of bubble expansion, the effects of material strength and failure, a more accurate accounting of the partial reflections of stress waves at the surface of the bubble, and an accurate equation of state. In addition, we presented a description of the interface instability expected during bubble evolution.

Three components of the physics contained in the ERM were benchmarked against LATIS simulations—acoustic radiation, material strength and failure, and interface instability. Good agreement was found for all three. Taking into account partial reflection of the acoustic wave at the bubble interface is important to find agreement between the ERM and LATIS. There is a factor of 2 or more discrepancy in how much energy is radiated and about the same in maximum radius, if the reflection factor (F) is not included. The form of the reflection factor that we derived has been verified. Material strength and failure was found to act as an increased ambient pressure, with a value equal to the shear failure stress of the material. This is manifested as smaller maximum bubble radii and shorter bubble oscillation periods. The bubble was found to be significantly unstable to interface instabilities on collapse—the magnitude of the oscillation growing a decade per collapse. With such growth, it is unlikely that bubbles generated by optical fibers will be able to bounce more than a few times as would a strictly spherical bubble.

It was found that the ERM model executed 300 times faster than the compressible hydrodynamic simulation code on equivalent computers. The extended Rayleigh model has proven accurate and fast. We suggest that it will be useful for quick calculations to aid in the design of devices using laser generated vapor bubbles.

ACKNOWLEDGMENTS

This work was performed under the auspices of the U.S. Department of Energy by the University of California Lawrence Livermore National Laboratory under Contract No. W-7405-Eng-48. One of the authors (M.E.G.) would like to acknowledge the support of a U.S. Department of Energy Distinguished Postdoctoral Fellowship and the support of the Shell E&P Technology Company.

APPENDIX: DERIVATION OF EXTENDED BUBBLE DYNAMICS EQUATION

In this Appendix an equation for the temporal evolution of a bubble is derived. This equation is a second order ODE for the bubble radius as a function of time. What differentiates this equation from previous work is a more complete treatment of the generation of the pressure wave. This more complete treatment is necessary to have agreement between

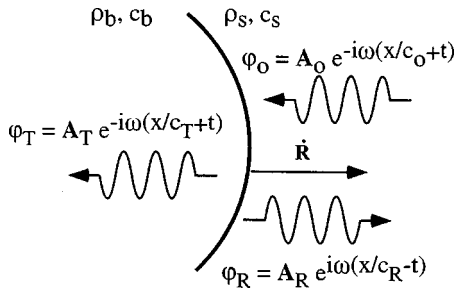


FIG. 18. The scattering of a wave by a moving interface.

the ERM and LATIS. The Kirkwood–Bethe hypothesis is used so that the equation will be valid for weak shocks [that is bubble wall Mach number $=\dot{R}/c_s \leq O(1)$]. The equation is not linearized in terms of the parameter $\dot{R}/c_s \ll 1$ (that is, it is not reduced to the acoustic wave limit). The weak shock is also allowed to both transmit and reflect at the bubble boundary. Both the weak shock nonlinearity and the partial transmission of the shock into the bubble are necessary to have good agreement between the ERM and LATIS. The derivation closely follows that of Knapp *et al.*⁵ The following discussion will focus on the essence of the derivation and will highlight the additions.

The starting point is the continuity equation

$$\frac{2u}{r} + \frac{\partial u}{\partial r} = -\frac{1}{c^2} \frac{dh}{dt}, \quad (\text{A1})$$

the momentum equation

$$\frac{du}{dt} = -\frac{\partial h}{\partial r}, \quad (\text{A2})$$

and the wave equation

$$\left(\frac{\partial}{\partial t} + (c+u) \frac{\partial}{\partial r} \right) \left(r \left(h + \frac{u^2}{2} \right) \right) \Big|_{r=R} = \frac{r}{c} \frac{dh}{dt} (1-F)(c-u), \quad (\text{A3})$$

where r is the radius, u is the radial fluid velocity, c is the sound velocity, and h is the enthalpy. The form of the left-hand side results from the Kirkwood–Bethe hypothesis, as discussed in the text. The form of the right-hand side is hypothesized subject to the requirement that it correctly accounts for the partial reflection of the in-going shock in the limit of small Mach number. If $F=1$, (total reflection) the right-hand side of Eq. (A3) equals 0 and Eq. (A3) reduces to the one found in Knapp *et al.*⁵ This hypothesis needs to be verified by comparison to detailed dynamic simulations.

The reflection factor F is determined by analyzing the geometry of the scattering of a wave by a moving interface (see Fig. 18). In this figure $u = \nabla \varphi$. Using continuity of pressure at the boundary

$$\rho_s \frac{\partial}{\partial t} (\varphi_o + \varphi_R) = \rho_b \frac{\partial}{\partial t} \varphi_T, \quad (\text{A4})$$

and continuity of speed at the boundary

$$\frac{\partial}{\partial x} (\varphi_o + \varphi_R) = \frac{\partial}{\partial x} \varphi_T, \quad (\text{A5})$$

along with the relationships

$$c_o = c_s - \dot{R}, \quad c_R = c_s + \dot{R}, \quad c_T = c_b - \dot{R},$$

the following equation is derived for the reflection factor:

$$F = \frac{1}{2} \left(1 - \frac{A_R}{A_o} \right) = \frac{\rho_s - \rho_b \dot{R} \left(\frac{c_b - \dot{R}}{c_s^2 - \dot{R}^2} \right)}{\rho_b \frac{c_b - \dot{R}}{c_s + \dot{R}} + \rho_s}. \quad (\text{A6})$$

Now Eqs. (A1)–(A3) can be combined and the result evaluated at $r=R$ to give

$$R \ddot{R} (1 - \dot{R}/c_s) + \frac{3}{2} \dot{R}^2 (1 - \dot{R}/3c_s) = h(1 + \dot{R}/c_s) + F \frac{R}{c_s} \dot{h} (1 - \dot{R}/c_s). \quad (\text{A7})$$

An implicit assumption in this derivation is the neglect of the transmitted wave generating a secondary reflected and transmitted waves after being reflected at the bubble center. These multiple reflections only contribute to the tail of the outgoing wave because they are time delayed by at least $2R/c_b$. Furthermore, the bubble expansion traps the ingoing wave inside the bubble via the reduction in the bubble density. Therefore, the contributions of the reflected waves have been ignored in the derivation of Eq. (A7).

¹K. W. Gregory, in *Interventional Cardiology*, edited by E. J. Topol (Sanders & Co., New York, 1994), p. 892; A. Vogel, S. Busch, K. Jungnickel, and R. Birngruber, *Lasers Surg. Med.* **15**, 32 (1994); T. G. van Leeuwen, E. D. Jansen, M. Motamedi, C. Borst, and A. J. Welch, in *Optical-Thermal Response of Laser-Irradiated Tissue*, edited by A. J. Welch and M. J. C. Van Gemert (Plenum, New York, 1995), p. 709; A. Vogel, R. Engelhardt, U. Behnle, and U. Parlitz, *Appl. Phys. B: Photophys. Laser Chem.* **62**, 173 (1996); A. Vogel and U. Parlitz, *J. Acoust. Soc. Am.* **100**, 148 (1996); U. Sathyam, A. Shearin, and S. Prahl, *Proc. SPIE* **2671**, 28 (1996); M. Strauss, R. A. London, M. E. Glinsky, P. A. Amendt, D. J. Maitland, D. S. Bailey, D. A. Young, and S. L. Jacques, *ibid.* **2671**, 11 (1996); D. Palanker, I. Turovets, and A. Lewis, *ibid.* **2975**, 351 (1997).

²A. Vogel and W. Lauterborn, *J. Acoust. Soc. Am.* **84**, 719 (1988); E. J. Chapyak, R. P. Godwin, S. A. Prahl, and H. Shangguan, *Proc. SPIE* **2970**, 28 (1997); R. P. Godwin, E. J. Chapyak, S. A. Prahl, and H. Shangguan, *ibid.* **3245**, 4 (1998); E. J. Chapyak and R. P. Godwin, *ibid.* **3245**, 12 (1998).

³Lord Rayleigh, *Philos. Mag.* **34**, 94 (1917).

⁴M. Plesset, *J. Appl. Mech.* **16**, 277 (1949); F. R. Gilmore, *California Institute of Technology*, Hydrodynamics Laboratory Report No. 26-4, 1950; L. Trilling, *J. Appl. Mech.* **23**, 14 (1952); R. Hickling and M. S. Plesset, *Phys. Fluids* **7**, 7 (1964).

⁵R. T. Knapp, J. W. Daily, and F. G. Hammitt, *Cavitation* (McGraw–Hill, New York, 1970), pp. 95–151; L. D. Landau and E. M. Lifshitz, *Fluid Mechanics*, 2nd ed. (Pergamon, London, 1970), pp. 251–312; M. S. Plesset and A. Prosperetti, *Annu. Rev. Fluid Mech.* **9**, 145 (1977).

⁶W. Lauterborn, *J. Acoust. Soc. Am.* **59**, 283 (1976); A. Prosperetti, L. A. Crum, and K. W. Commander, *ibid.* **83**, 502 (1988); W. Lauterborn and U. Parlitz, *ibid.* **84**, 1975 (1988).

⁷B. P. Barber and S. J. Putterman, *Phys. Rev. Lett.* **69**, 3839 (1992); R. Lofstedt, B. P. Barber, and S. J. Putterman, *Phys. Fluids A* **5**, 2911 (1993); C. C. Wu and P. H. Roberts, *Phys. Rev. Lett.* **70**, 3424 (1993); W. Moss, D. Clarke, J. White, and D. Young, *Phys. Fluids* **6**, 2979 (1994); P. H. Roberts and C. C. Wu, *Phys. Lett. A* **213**, 59 (1996).

⁸J. G. Kirkwood and H. A. Bethe, OSRD Report No. 588, 1942; R. H. Cole, *Underwater Explosions* (Princeton University Press, Princeton, 1948).

⁹L. D. Landau and E. M. Lifshitz, *Theory of Elasticity*, 2nd ed. (Pergamon, London, 1970), pp. 20–21.

¹⁰Lord Rayleigh, *Scientific Papers* (Cambridge University Press, Cambridge, 1900), Vol. II, p. 200; G. I. Taylor, *Proc. R. Soc. London, Ser. A*

- 201**, 192 (1950); M. S. Plesset, *J. Appl. Phys.* **25**, 96 (1954); S. Chandrasekhar, *Hydrodynamic and Hydromagnetic Stability* (Oxford University Press, Oxford, 1961), Chap. 10.
- ¹¹M. E. Glinsky, R. A. London, G. B. Zimmerman, and S. L. Jacques, *Proc. SPIE* **2391**, 262 (1995); R. A. London, M. E. Glinsky, G. B. Zimmerman, D. S. Bailey, D. C. Eder, and S. L. Jacques, *Appl. Opt.* **36**, 9068 (1997).
- ¹²G. B. Zimmerman and W. L. Kruer, *Plasma Phys. Controlled Fusion* **11**, 82 (1975).
- ¹³M. Wilkins, in *Methods in Computational Physics*, edited by B. Alder, S. Fernbach, and M. Rotenberg (Academic, New York, 1964), Vol. 31, p. 211.
- ¹⁴R. M. More, K. H. Warren, D. A. Young, and G. B. Zimmerman, *Phys. Fluids* **31**, 3059 (1988).
- ¹⁵L. Haar, J. S. Gallagher, and G. S. Kell, *NBS/NRC Steam Tables* (McGraw-Hill, New York, 1984).
- ¹⁶P. Amendt, M. Strauss, R. A. London, M. E. Glinsky, D. J. Maitland, P. M. Celliers, S. R. Visuri, D. S. Bailey, D. A. Young, and D. Ho, *Proc. SPIE* **2975**, 362 (1997).
- ¹⁷H. Kull, *Phys. Rep.* **206**, 197 (1991).